

## Eastern-Boundary Contribution to the Residual and Meridional Overturning Circulations

PAOLA CESSI, CHRISTOPHER L. WOLFE, AND BONNIE C. LUDKA

*Scripps Institution of Oceanography, University of California, San Diego, La Jolla, California*

(Manuscript received 7 January 2010, in final form 12 May 2010)

### ABSTRACT

A model of the thermocline linearized around a specified stratification and the barotropic linear wind-driven Stommel solution is constructed. The forcings are both mechanical (the surface wind stress) and thermodynamical (the surface buoyancy boundary condition). The effects of diapycnal diffusivity and of eddy fluxes of buoyancy, parameterized in terms of the large-scale buoyancy gradient, are included. The eddy fluxes of buoyancy are especially important near the boundaries where they mediate the transport in and out of the narrow ageostrophic down-/upwelling layers. The dynamics of these narrow layers can be replaced by effective boundary conditions on the geostrophically balanced flow. The effective boundary conditions state that the residual flow normal to the effective coast vanishes. The separate Eulerian and eddy-induced components may be nonzero. This formulation conserves the total mass and the total buoyancy while permitting an exchange between the Eulerian and eddy transport of buoyancy within the down-/upwelling layers. In turn, this exchange allows buoyancy gradients along all solid boundaries, including the eastern one. A special focus is on the buoyancy along the eastern and western walls since east–west buoyancy difference determines the meridional overturning circulation.

The inclusion of advection of buoyancy by the barotropic flow allows a meaningful distinction between the meridional and the residual overturning circulations while retaining the simplicity of a linear model. The residual flow in both meridional and zonal directions reveals how the subsurface buoyancy distribution is established and, in particular, how the meridional buoyancy gradient is reversed at depth. In turn, the horizontal buoyancy gradient maintains stacked counterrotating cells in the meridional and residual overturning circulations. Quantitative scaling arguments are given for each of these cells, which show how the buoyancy forcing, the wind stress, and the diapycnal and eddy diffusivities, as well as the other imposed parameters, affect the strength of the overturn.

### 1. Introduction

The meridional overturning circulation (MOC) is forced by a combination of buoyancy, through differential heating and freshwater fluxes at the surface, and by wind stress. Both forcing mechanisms contribute to the establishment of the vertical and horizontal subsurface buoyancy gradients (Young and Rhines 1982; Luyten et al. 1983; Salmon 1990; Samelson and Vallis 1997).

One way to efficiently monitor the MOC is to observe the baroclinic component of the pressure (i.e., the buoyancy) at the eastern and western boundaries: these endpoint values control the geostrophic transport of the zonally integrated flow (Hirschi and Marotzke 2007;

Kanzow et al. 2008). Preliminary results from the Rapid Climate Change–Meridional Overturning Circulation and Heatflux Array (RAPID–MOCHA) observational program indicate that this is an effective monitoring strategy (Kanzow et al. 2009; Rayner et al. 2010, manuscript submitted to *Deep-Sea Res.*). Unfortunately, these observations are limited to the MOC, which is the transport of mass (or volume in a Boussinesq fluid). Another quantity of interest is the residual overturning circulation (ROC), which measures the transport of temperature and other tracers by all components of the flow. The ROC would be more useful to monitor than the MOC since it measures the transport of heat. However, there is no obvious way to measure the ROC using endpoint values only.

Although various scalings have been proposed that relate the strength of the MOC to external parameters (cf. Vallis 2000), we still do not have a coherent picture that unifies all the scalings. Little attention has been paid

---

*Corresponding author address:* Paola Cessi, UCSD, Mail Code 0213, 9500 Gilman Drive, La Jolla, CA 92093-0213.  
E-mail: pcessi@ucsd.edu.

to the scaling of the ROC. There are two major difficulties in providing a comprehensive scalings for either the MOC or the ROC. First, it is necessary to understand how the large-scale oceanic stratification and flow are established. Because the oceanic large-scale stratification is forced at the top, there are several processes, sometimes competing, that distribute the surface buoyancy signal down the water column. Second, knowledge of the fluctuating components of temperature and velocity are needed, and these fields are concentrated at the mesoscales. The contribution of the eddy component to the buoyancy flux has often been neglected in theories of the large-scale stratification.

One of the processes that transfer the surface buoyancy gradients downward is ventilation (Luyten et al. 1983). Ventilation establishes buoyancy gradients only in the subtropical regions where the Ekman pumping is downward. The effectiveness of ventilation is controlled by the extent to which the mean potential vorticity is conserved along the mean flow: simulations that include the spontaneous development of time-dependent eddies show that the large-scale mean potential vorticity is, in fact, not well conserved because the divergence of eddy fluxes is as important as the divergence of the mean flux of potential vorticity (Cox and Bryan 1984). When eddies are important, potential vorticity homogenization (Rhines and Young 1982; Young and Rhines 1982; Pedlosky and Young 1983) is more prominent than ventilation. Neither homogenization nor ventilation explains the horizontally averaged stratification: the quasigeostrophic theories are pivoted around a specified basic stratification, and the ventilation theories require the depth of the isopycnals to be known on the eastern boundary; that is, the stratification needs to be prescribed all along the eastern boundary.

At the opposite spectrum of the “ideal” theories summarized above are the “diffusive” scalings proposed by Welander (1971) and Gill (1985, hereafter G85), which invoke diapycnal diffusion as the primary process that transfers buoyancy downward.

A partial reconciliation of the diffusive and potential vorticity conserving paradigms is achieved by considering that the diffusive scaling applies in an internal boundary layer below the ventilated/homogenized thermocline (Stommel and Webster 1962; Young and Ierley 1986; Salmon 1990; Samelson and Vallis 1997). However, this framework is appropriate only in the subtropical regions where there is downward Ekman pumping. In the subpolar region, where the maximum of the Eulerian overturning circulation is found, the depth of the thermocline cannot be determined by ventilation: either diffusion (e.g., in the mixed layer) or remote processes must control the dynamics. All of the above theories neglect the contribution to the buoyancy gradients from the eastern

boundary. In this work, we show how buoyancy gradients are established on the eastern boundary and to what extent the eastern boundary buoyancy contributes to the time-averaged MOC and ROC.

Recent modeling work (Wolfe and Cessi 2010) has revealed that the existence of a reentrant portion in the World Ocean is essential to establish deep stratification: the westerly winds in the Antarctic Circumpolar Current (ACC) region induce an ageostrophic meridional flow that overturns the isopycnals very effectively. This overturn is modestly opposed by the restratification due to baroclinic eddies, which are less effective at restratification than the basinwide gyres supported by meridional boundaries. The net result is that the stratification obtained in a reentrant geometry reaches much farther down the water column than in a fully enclosed basin geometry. The deep stratification established in the reentrant region is then communicated to the enclosed portions of the World Ocean by the residual circulation. It is thus meaningful to consider the circulation and buoyancy distribution that ensues in the closed portion of the domain, given the deep stratification emanating from the ACC region (cf. Gnanadesikan 1999).

In this work we attempt to offer a comprehensive, albeit simplified, picture of both the MOC and ROC in the context of a single hemisphere in a fully enclosed domain. We consider the simplest model with specified stratification  $N^2$ , that is, the planetary geostrophic equations, with buoyancy linearized around a given uniform  $N^2$  as in G85.

We also include a parameterized form of eddy-flux divergence since this is an important process for both the MOC and the ROC, especially near the boundaries. In particular, eddy fluxes of buoyancy relax the condition that the normal component of the geostrophic flow must vanish at the eastern boundary. As in previous work (Salmon 1986; Cessi and Wolfe 2009, hereafter CW09), we include the contribution of side upwelling and downwelling layers. The net effect of the mass and buoyancy transport in these thin layers on the interior flow can be described by an “effective boundary condition,” derived in the following section, which applies to both the momentum and the buoyancy equations. The derivation has previously been given in CW09, but here we emphasize that this is the correct boundary condition that should be used in coarse-resolution models in which the eddy fluxes of tracers are parameterized.

The effective boundary condition allows horizontal buoyancy gradients along the eastern boundary, which is a major step in the direction of greater realism for this idealized class of models. These gradients support a counterrotating overturning cell below the main thermally direct MOC. This cell exists because of the reversed

subsurface horizontal gradient created by the interaction of the thermally direct MOC with the deep stratification. An important conclusion is that without buoyancy gradients along the eastern boundary this cell would not exist.

Advection of buoyancy by the barotropic flow, which can be calculated separately from the buoyancy field, is also allowed, a process that was neglected in CW09. Barotropic advection is not as comprehensive as the advection by the total flow, but it captures a large fraction of the buoyancy advection while still dealing with a linear problem. Importantly and instructively, consideration of advection by the barotropic flow allows a meaningful distinction between the MOC and the ROC. We find that the advection by the barotropic flow opposes the poleward transport by the MOC in the subtropical gyre and reinforces it in the subpolar gyre. The net result is a shift of the maximum of the ROC poleward relative to the MOC. This shift is also found in the eddy-resolving computations reported in Wolfe and Cessi (2010).

**2. The model equations and boundary conditions**

We employ the planetary geostrophic equations, incompressible and hydrostatic, with buoyancy linearized around a prescribed vertical stratification  $b_o(z)$ , such that  $db_o/dz = N^2(z)$ , and is advected by the barotropic flow only. Then, the baroclinic velocity  $u, v, w$ , and associated perturbation pressure  $p$  and buoyancy  $b$  satisfy

$$-f v = -p_x + \tau_z \cdot \mathbf{x}, \tag{1}$$

$$f u = -p_y + \tau_z \cdot \mathbf{y}, \tag{2}$$

$$0 = -p_z + b, \tag{3}$$

$$0 = u_x + v_y + w_z, \tag{4}$$

and

$$J(\psi, b) + w N^2 = \kappa_e \nabla^2 b + \kappa_v b_{zz}. \tag{5}$$

The streamfunction  $\psi$  characterizes the barotropic velocity and is determined independently of the buoyancy through the Sverdrup relation

$$\beta \psi_x = \frac{1}{H} \text{curl} \tau|_{z=0} - r \nabla^2 \psi, \tag{6}$$

$$\psi = 0 \quad \text{at } x = 0, x_e, y = 0, L,$$

where  $H$  is the depth of the ocean and  $r$  is the small coefficient of bottom friction. In (1)–(4), the baroclinic velocity has zero vertical average and  $f = \beta y$ .

Large-scale theories of the thermocline (Colin de Verdière 1989; Salmon 1990; Samelson and Vallis 1997) include advection of buoyancy by all components of the large-scale flow, resulting in a nonlinear problem. By considering advection by the barotropic flow only, the problem is linear and captures the largest contribution to buoyancy advection. This is because, by thermal wind balance, the horizontal velocity of each vertical mode is orthogonal to the buoyancy gradient of the same mode so that only advection by a different vertical mode is possible. Since the amplitude of each vertical mode decays with mode number, the largest interaction is between advection by the barotropic velocity of the first baroclinic mode for buoyancy (Smith and Vallis 2001).

Eddy fluxes of buoyancy, parameterized as down-gradient diffusion (Gent and McWilliams 1990), are explicitly included. Because buoyancy is linearized around  $b_o(z)$ , that is, the isopycnals are horizontal to a first approximation, isopycnal eddy fluxes are also approximately horizontal: this is the first term on the rhs of (5). In other words, in this linearized model, we neglect the vertical component of the buoyancy eddy fluxes,  $\overline{w'b'}$  (cf. the discussion in CW09).

The system (1)–(5) is solved in a closed domain bounded by solid walls at  $x = 0, x_e$  and  $y = 0, L$ . The bottom, located at  $z = -H$ , is flat, and we make the rigid-lid approximation, so the surface is at  $z = 0$ . Previous work on the planetary geostrophic set (1)–(5) (Salmon 1990; Samelson and Vallis 1997) has demonstrated that it is not possible to impose no-normal flow for  $u$  and  $v$  and no-normal flux of buoyancy on the horizontal boundaries without adding additional physics.<sup>1</sup> Salmon (1990) adds nonhydrostatic effects and Samelson and Vallis (1997) add hyperdiffusion of buoyancy. In the following we argue that a single effective boundary condition for both the normal flow and the buoyancy flux can be specified, which takes into account the effect on the interior of unresolved viscous, nonhydrostatic, down-/upwelling boundary layers. Notice that we consider a completely inviscid momentum balance for the interior baroclinic flow so that, below the Ekman layer, the baroclinic velocity is in geostrophic balance everywhere. The effective boundary condition requires that only the residual normal flow, that is, the sum of the Eulerian plus eddy-induced flow, vanishes at the outer edge of the down-/upwelling boundary layer, but not each separate component.

We derive the effective boundary condition for a general form of the eddy fluxes of buoyancy and then

<sup>1</sup> The addition of bottom drag or inertia does not solve this problem.

apply it to the downgradient diffusion parameterization used in (5). Thus, we consider the general buoyancy balance

$$\overline{u}b_x + \overline{v}b_y + \overline{w}b_z + (\overline{u'b'})_x + (\overline{v'b'})_y + (\overline{w'b'})_z = \kappa_v \overline{b}_{zz}, \quad (7)$$

where the overbar denotes a time average and the prime departure from the time average. The mass balance for both barred and prime quantities is (4).

In the thin boundary layer next to an eastern wall,  $x = x_e$ , the gradients of the mean velocities,  $\overline{u}_x$  and  $\overline{v}_x$ , are large and so is  $\overline{w}$ . However,  $\overline{b}_x$  and  $v$  are not large because  $b$  (and the pressure) is almost constant in the boundary layer (cf. Barcilon and Pedlosky 1967; Pedlosky 1969; CW09). In other words, in the viscous, nonhydrostatic boundary layer the normal velocity changes to leading order, but not the pressure or buoyancy, only their gradients. As shown in CW09, the mean vertical velocity  $\overline{w}$  also becomes large; similarly, the eddy-flux divergence of buoyancy  $(\overline{u'b'})_x$  is large. Thus, the dominant mass and buoyancy balances in the thin down-/upwelling boundary layer are

$$\overline{u}_x + \overline{w}_z \approx 0 \quad (8)$$

and

$$\overline{w}b_z + (\overline{u'b'})_x \approx 0. \quad (9)$$

We now integrate (8) across the boundary layer, using the condition that  $\overline{u} = 0$  on the solid wall:

$$\overline{u}|_{x=x_e-\delta_{bl}} \approx \int_{x_e-\delta_{bl}}^{x_e} \overline{w}_z dx. \quad (10)$$

Integrating (9) across the boundary layer of width  $\delta_{bl}$ , using the condition that  $\overline{u} = \overline{u'b'} = 0$  on the solid wall, we find

$$\int_{x_e-\delta_{bl}}^{x_e} \overline{w} dx \approx \frac{\overline{u'b'}}{\overline{b}_z} \Big|_{x=x_e-\delta_{bl}}. \quad (11)$$

In other words, the amount of fluid integrated over the up/downwelling layer is proportional to the eddy flux of buoyancy at the outer edge of the boundary layer, that is, at the ‘‘effective coast’’ as far as the interior fluid is concerned.

Substituting (11) into (10) we finally arrive at the result

$$\overline{u} = \left( \frac{\overline{u'b'}}{\overline{b}_z} \right)_z \quad \text{at } x = x_e - \delta_{bl}, \quad (12)$$

which is the effective boundary condition to be used at the effective boundary instead of the condition  $\overline{u} = u' = 0$ .

The above arguments can be repeated on any boundary, and the effective boundary condition applied to the normal velocity at the seaward edge of the boundary layer, that is, at the effective coast, is

$$\overline{\mathbf{u}} \cdot \mathbf{n} = \left( \frac{\overline{\mathbf{u}'b'} \cdot \mathbf{n}}{\overline{b}_z} \right)_z, \quad (13)$$

where  $\mathbf{n}$  is the outward unit vector normal to the boundary. The rhs of (13) is the negative of the eddy-induced (or ‘‘bolus’’) flow normal to the boundary. Thus, (13) states that the residual flow vanishes on the boundary, but not the mean and eddy component separately. Notice that the final boundary condition (13) is independent of the boundary layer width or any other detail of the viscous dynamics of the up/downwelling layers. The effective boundary condition is now applied to the inviscid momentum equation because viscosity only acts within the boundary layer.

Notice that the effective boundary condition (13) applies only to the baroclinic component of the flow: both terms in the equality must have zero vertical average so as to ensure mass conservation. The barotropic flow is unaffected by the up/downwelling dynamics of the side boundary layers and satisfies the no-normal flow condition. Figure 1 diagnoses the two sides of (13) from the eddy-resolving simulation described in Wolfe and Cessi (2010) and shows agreement, except in regions of convective adjustment, where mixing is not negligible, and near the equator. Because of the limited resolution of the model, the diagnostic is evaluated three points from the eastern boundary, that is, 16.3 km offshore. This is a distance much larger than the typical width of nonhydrostatic turbulent boundary layers in the ocean, and subdominant terms that should vanish in the limit as  $\delta_{bl} \rightarrow 0$  do not. Preliminary calculations show that the agreement improves as the grid size is reduced.

In coarse-resolution ocean models the eddy flux of buoyancy is parameterized in terms of the large-scale gradient of buoyancy (Gent and McWilliams 1990) so that (13) is a relation between the wall-normal horizontal component of the velocity and the horizontal buoyancy gradient normal to the boundary:

$$\overline{\mathbf{u}} \cdot \mathbf{n} = - \left( \frac{\kappa_e \nabla \overline{b} \cdot \mathbf{n}}{\overline{b}_z} \right)_z. \quad (14)$$

It is easy to show that the above boundary condition conserves the total buoyancy by integrating (5) over the

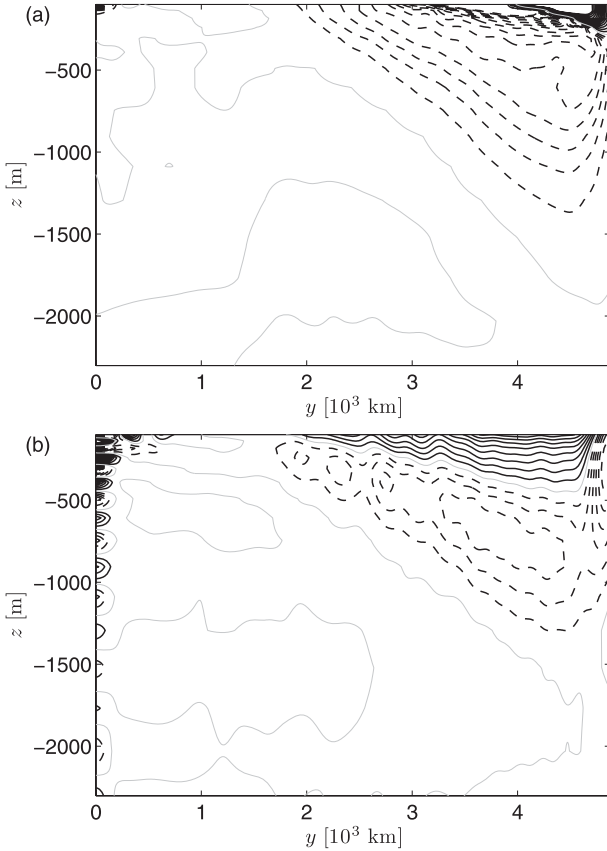


FIG. 1. The eddy buoyancy flux  $(\overline{u' b' / b_z})_z$  and  $\overline{u}_{bc}$  16.3 km off the eastern boundary for an eddy-resolving computation (the subscript “bc” refers to the baroclinic component of the flow, with zero vertical average). Smoothing is applied in the  $y$  direction using a Gaussian filter with a half-width of 60 km to remove grid noise excited by hydrostatic convection. The parameters of the model are described in Wolfe and Cessi (2010).

domain and applying (14) on the lateral boundaries (and  $w = 0$  on the top and bottom).

We believe that (14) is the coarse-resolution boundary condition that should be applied to the baroclinic (zero-vertical average) component of the horizontal velocity and to the buoyancy flux.<sup>2</sup> In other words, in coarse-resolution ocean models using parameterized eddy fluxes, (14) serves as the boundary condition for both momentum and buoyancy equations.

The need for a single lateral boundary condition relating the normal velocity  $\overline{\mathbf{u}} \cdot \mathbf{n}$  to the buoyancy flux

<sup>2</sup>The requirement that both sides of (14) have zero vertical average implies  $\kappa_e = 0$  at  $z = 0, -H$ . This condition is implemented in most ocean models. In this study, we take  $\kappa_e$  to be constant and thus in general do not satisfy the condition that the eddy streamfunction vanishes at  $z = 0, -H$ . Application of (14) to mass conservation requires that on the boundary  $0 = \int_{-H}^0 dz \oint \mathbf{u} \cdot \mathbf{n} dl = -\kappa_e N^{-2} \oint \nabla b \cdot \mathbf{n} \Big|_{-H}^0 dl$  and this vanishes for the particular choice (20).

$\kappa_e \nabla b \cdot \mathbf{n}$ , is evident when the system (1)–(5) is reduced to a single equation in terms of the buoyancy. Forming the vertical derivative of the potential vorticity (PV) equation, this system is

$$\frac{\beta}{f^2} b_x + \left[ \frac{J(\psi, b)}{N^2} \right]_{zz} = \left( \frac{\kappa_e \nabla^2 b + \kappa_v b_{zz}}{N^2} \right)_{zz} + \text{curl} \left( \frac{\boldsymbol{\tau}_{zz}}{f} \right). \tag{15}$$

The effective boundary condition can be expressed in terms of the buoyancy alone by taking the vertical derivative of (14) and using (1) and (2); that is,

$$f \left( \frac{\kappa_e \nabla b \cdot \mathbf{n}}{N^2} \right)_{zz} = (\nabla b - \boldsymbol{\tau}_{zz}) \cdot \mathbf{s}, \tag{16}$$

where  $\mathbf{n}$  and  $\mathbf{s} \equiv \mathbf{z} \times \mathbf{n}$  are the outward normal and tangent unit vectors on the boundary, respectively. Thus, the buoyancy gradient along the boundary is proportional to the buoyancy gradient across the effective boundary, maintained by the eddy flux of buoyancy.

Boundary conditions need also to be specified at the top and bottom boundaries. Here, we specify the buoyancy perturbation at the top and assume no signal at the bottom. Usually, it is the flux of buoyancy,  $-\kappa_v b_z$ , that is required to vanish at the bottom. However, we will show that the buoyancy signal decays rapidly away from the top surface so that both  $b$  and  $b_z$  vanish at the bottom. Finally, the vertical velocity is required to vanish at  $z = 0, -H$ . In summary, the vertical boundary conditions are

$$b = b_s(x, y), \quad J(\psi, b_s) - \kappa_e \nabla^2 b_s - \kappa_v b_{szz} = 0 \quad \text{at } z = 0 \tag{17}$$

and

$$b = \kappa_v b_{zz} = 0 \quad \text{at } z = -H. \tag{18}$$

In the following we will use the forcing:

$$b_s = B_0 B(y), \quad \boldsymbol{\tau} = (\tau_0 \hat{\tau}(y), 0) \tag{19}$$

with

$$B(y) = \cos \pi \frac{y}{L} \tag{20}$$

and

$$\boldsymbol{\tau} = e^{z/d} \boldsymbol{\sigma}(y) = e^{z/d} \left( -\cos \frac{3\pi y}{2L} + 0.8 \exp \frac{-y^2}{2(0.09L)^2} \right). \tag{21}$$

This is the same forcing applied to the eddy-resolving computations that we are using for comparison (cf. Wolfe and Cessi 2010). Figure 2 shows  $B$  and  $\tau$  as a function of  $y$ .

The final formulation (15) is similar to that of CW09 except that here we include horizontal advection of buoyancy, although limited to the barotropic flow. We also apply the boundary conditions (16) on all four lateral boundaries, in a fully closed domain, rather than assuming no net meridional flow at  $y = 0, L$ , as in CW09. The boundary conditions used by CW09, where the buoyancy is assumed constant along the meridional boundaries, are recovered in the limit where  $x_e \ll L$ , and  $\tau(0) = \tau(L) = 0$ .

### 3. Nondimensionalization

We scale the amplitude of the solution with the surface buoyancy  $B_0$ . The PV dynamics (15) together with the effective boundary conditions (16) provide the natural scales of the solution, both horizontal and vertical. Thus, we use the following nondimensionalization (indicated by carets):

$$b = B_0 \hat{b}, \quad x = l\hat{x}, \quad y = L\hat{y}, \quad z = h\hat{z}, \quad \psi = \frac{\tau_0 l}{\beta H L} \hat{\psi}, \tag{22}$$

where  $l$  and  $h$  are

$$l \equiv \left( \frac{\beta L^2 \kappa_e^2}{N^2 \kappa_v} \right)^{1/3}, \quad h \equiv \left( \frac{\beta L^2 \sqrt{\kappa_e \kappa_v}}{N^2} \right)^{1/3}. \tag{23}$$

This is the same ‘‘canonical scaling’’ used in CW09, which characterizes the intrinsic scales of the solution. For oceanographically relevant parameters  $h \sim 300$  m and  $l \sim 1000$  km (cf. Table 1); that is, both scales are less than the domain scales but larger than a thin boundary layer. Assuming that  $N^2$  is constant, the vorticity equation becomes

$$\frac{\hat{b}_{\hat{x}}}{\hat{y}^2} + \epsilon J(\hat{\psi}, \hat{b}_{\hat{z}\hat{z}}) = (\hat{\nabla}^2 \hat{b} + \hat{b}_{\hat{z}\hat{z}})_{\hat{z}\hat{z}} - \mu \left( \frac{\hat{\tau}_{\hat{z}\hat{z}}}{\hat{y}} \right)_{\hat{y}}. \tag{24}$$

The nondimensional barotropic vorticity is

$$\hat{\psi}_{\hat{x}} = -\sigma_{\hat{y}} - \frac{\delta_s}{l} \hat{\nabla}^2 \hat{\psi}, \tag{25}$$

where  $\sigma$  is the nondimensional wind stress at the surface given in (21) and  $\delta_s = r/\beta$  is the Stommel (1948) boundary layer width. The nondimensional effective boundary conditions become

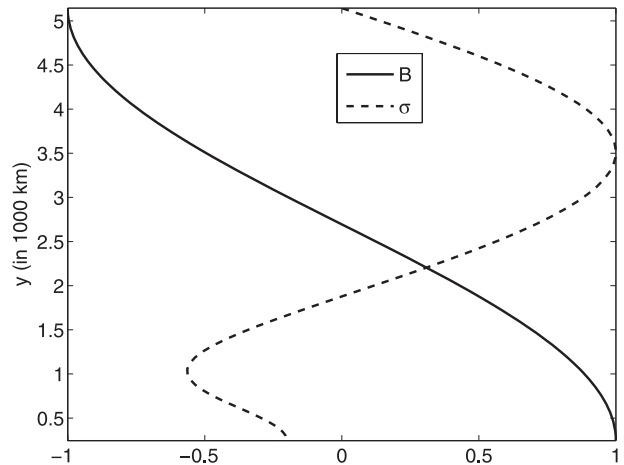


FIG. 2. The shapes of the surface buoyancy  $B$  (solid) and zonal wind stress  $\sigma$  (dashed) are shown as a function of  $y$ . Both quantities are in nondimensional units. Notice that there is no wind stress or buoyancy gradient at the northern boundary so that there is very little upwelling there. There is easterly wind at the southern boundary, which causes local upwelling.

$$\hat{b}_{\hat{y}} = \hat{y} \hat{b}_{\hat{x}\hat{z}\hat{z}} \quad \text{at} \quad \hat{x} = 0, X_e \tag{26}$$

and

$$\hat{b}_{\hat{x}} = \left[ -\left( \frac{l}{L} \right)^2 \hat{y} \hat{b}_{\hat{y}} + \mu \hat{\tau} \right]_{\hat{z}\hat{z}} \quad \text{at} \quad \hat{y} = 0, 1. \tag{27}$$

The solution is determined by the following parameters:

$$\mu \equiv \frac{\tau_0 l}{B_0 h^2}, \quad \epsilon \equiv \frac{\tau_0 l^2}{\beta L^2 H \kappa_e}, \quad X_e \equiv x_e / l. \tag{28}$$

Additionally, the aspect ratio  $l/L$  enters in the definition of the nondimensional Laplacian<sup>3</sup>,  $\hat{\nabla}^2 \equiv \partial_{\hat{x}\hat{x}} + (l/L)^2 \partial_{\hat{y}\hat{y}}$ .

#### Other dynamical scales

The canonical scaling (23) shows that, in the absence of an externally imposed zonal or vertical scale, the buoyancy gradient is naturally established over a depth  $h$  and an east–west length  $l$ . However, the surface forcing is imposed over the width of the whole basin,  $x_e \neq l$ . On the scale  $x_e$ , eddy diffusion is negligible and buoyancy acquires the vertical scale  $h_G$  identified in G85, such that

<sup>3</sup> In practice, we decrease the eddy diffusivity in the  $y$  direction by a further factor of 9 so that the aspect ratio  $l/L$  in (27) and in  $\hat{\nabla}^2$  is artificially decreased by a factor of 3. This choice mimics the finding in the eddy-resolving model that the eddy diffusivity along the northern boundary is much smaller than that along the eastern and western boundaries.

TABLE 1. Parameter values for the control calculation shown in Figs. 3, 4, 6, and 7. The buoyancy amplitude corresponds to a difference of 16°C, and the wind stress (divided by the density) corresponds to a momentum flux of 0.1 N m<sup>-2</sup>. With this choice for  $B_0$  the range of surface buoyancies is comparable to the range spanned by the prescribed stratification since  $N^2H = 1 \times 10^{-2}$ , violating the linearization assumption. We use these values to make quantitative comparisons with the results of our eddy-resolving computations.

External scales (m)	$L = 4.9 \times 10^6$	$x_e = 2.4 \times 10^6$	$H = 2400$	$d = 12$
External parameters	$\beta = 2.3 \times 10^{-11} \text{ m}^{-1} \text{ s}^{-1}$	$N = 2 \times 10^{-3} \text{ s}^{-1}$	$r = 1 \times 10^{-6} \text{ s}^{-1}$	
Diffusivities (m <sup>2</sup> s <sup>-1</sup> )	$\kappa_e = 1.2 \times 10^3$	$\kappa_v = 1 \times 10^{-4}$		
Intrinsic lengths (m)	$l = 1.2 \times 10^6$	$\delta_P = 9.2 \times 10^5$	$\delta_s = 4.2 \times 10^4$	
Intrinsic depths (m)	$h = 362 \text{ m}$	$h_G = 424$	$h_\psi = 158$	$h_v = 122$
Forcing amplitudes	$B_0 = 0.016 \text{ m}^2 \text{ s}^{-1}$	$\tau_0 = 1 \times 10^{-4} \text{ m}^2 \text{ s}^{-2}$		
Control parameters	$\mu = 0.06$	$\epsilon = 0.1$	$X_e = 1.9$	$l/L = 0.25$

$$h_G \equiv \left( \frac{\kappa_v \beta L^2 x_e}{N^2} \right)^{1/4}. \quad (29)$$

Thus, if  $x_e \gg l$ , the depth of the surface buoyancy signal at the western boundary is the Gill depth  $h_G > h$ . This implies that the baroclinic western boundary layer, where eddy-diffusion becomes important, is of width  $\delta_P < l$ , with

$$\delta_P \equiv \kappa_e L \left( \frac{\beta}{\kappa_v x_e N^2} \right)^{1/2}. \quad (30)$$

The scale  $\delta_P$  is one of the possible western boundary layer widths for the baroclinic component of the flow considered by Pedlosky (1969). The scaling (30) makes it clear that the width of the western boundary layer for the baroclinic flow is completely different than the width of the western boundary layer for the barotropic flow, which is Stommel’s scale  $\delta_s \equiv r/\beta$ . The former depends on the eddy diffusivity and the stratification, whereas the latter depends on the bottom drag. The scales  $h_G$ ,  $x_e$ , and  $\delta_P$  are the vertical and horizontal scales that dominate the subsurface buoyancy distribution because the surface forcing is imposed on the basin scale. At depth, the externally imposed scale is not relevant and the buoyancy field exhibits the intrinsic scales  $h$  and  $l$ .

With the barotropic advection characterized by  $\psi$ , we have an additional vertical scale  $h_\psi$ , which measures the deflection of the geostrophic contours from latitude lines by  $\psi$ , defined as

$$h_\psi \equiv \sqrt{\frac{\tau_0 x_e}{N^2 H}}. \quad (31)$$

This is the depth to which, in this formulation, the theory of Young and Rhines (1982) would predict homogenization of potential vorticity, that is, the vertical scale at which advection by  $\psi$  of vortex stretching [the second term on the lhs of (15)] balances advection by the baroclinic flow of planetary vorticity [the first term on the lhs

of (15)]. If both eddy and diapycnal diffusions were weak, then homogenization of potential vorticity would be expected in the region of closed potential vorticity contours. In the large-scale limit and if advection by all components of the flow were taken into account, then homogenization would occur in a “bowl” whose depth at the western boundary,  $h_v$ , scales as  $h_v \sim (\tau_0 x_e / N^2)^{1/3}$  (cf. Young and Rhines 1982) or, in the planetary-scale nonlinear regime, to a depth given by (cf. Pedlosky and Young 1983)

$$h_v = \left( \frac{\tau_0 x_e}{B_0} \right)^{1/2}. \quad (32)$$

The scalings for  $h_v$  and  $h_\psi$  coincide if we equate  $H$  with  $h_\psi$  in (31) (and  $N^2 = B_0/h_v$ ): in other words, if the vertical scale of the advecting flow and the vertical scale of the buoyancy coincide. Here, because only advection by the barotropic flow is included, the vertical scale of the homogenization bowl is smaller than that predicted by the large-scale nonlinear theory.

The essential point is that, for the parameter values given in Table 1,  $h_\psi < h_G$  and diapycnal diffusion dominates over advection. As shown in Table 1, for typical oceanic values  $h_v$  is at most of the same order as  $h_G$ , so diapycnal diffusivity would prevent homogenization even in the case where advection by the total flow is considered.

#### 4. The solution

##### a. Method of solution

The solution of (24) can be obtained by a Galerkin projection in vertical modes, with convergence accelerated by the addition of a particular solution that satisfies the boundary conditions on  $b$  at  $z = 0, -H$ :

$$\hat{b} = B(y) \left( 1 + \frac{\hat{z}}{H} \right) + \sum_{n=0}^{\infty} b_n(\hat{x}, \hat{y}) \sin(k_n \hat{z}), \quad \text{with} \quad (33)$$

$$k_n \equiv \frac{n\pi}{H},$$

where  $\hat{H} \equiv H/h$ . In terms of the vertical modes, the potential vorticity becomes

$$\begin{aligned} \partial_{\hat{x}} b_n + \hat{y}^2 k_n^2 [\hat{\nabla}^2 b_n - \epsilon \hat{J}(\hat{\psi}, b_n) - k_n^2 b_n] \\ = \frac{2}{H} k_n \hat{y}^2 \left[ \hat{\nabla}^2 B - \epsilon \hat{J}(\hat{\psi}, B) + \mu \left( \frac{\sigma}{\hat{y}} \right)_{\hat{y}=1} \frac{1}{1 + d^2 k_n^2} \right]. \end{aligned} \quad (34)$$

The system (34) is a set of second-order uncoupled PDEs in  $\hat{x}$  and  $\hat{y}$  that must be supplemented by the effective boundary conditions (26) and (27), projected onto the vertical sine modes; that is,

$$\begin{aligned} k_n^2 \hat{y} \partial_{\hat{x}} b_n + \partial_{\hat{y}} b_n &= \frac{2}{H k_n} B_{\hat{y}} \quad \text{at } \hat{x} = 0, X_e; \\ -\left(\frac{l}{L}\right)^2 \hat{y} k_n \partial_{\hat{y}} b_n + \partial_{\hat{x}} b_n &= \frac{2}{H} k_n \left[ \left(\frac{l}{L}\right)^2 \hat{y} B_{\hat{y}} - \frac{\mu \sigma}{1 + d^2 k_n^2} \right] \\ &\text{at } \hat{y} = 0, 1. \end{aligned} \quad (35)$$

The system (34) and (35) is discretized using Chebychev interpolating polynomials (Trefethen 2000), and the resulting matrix equation is inverted with MATLAB. The terms in the series in (34) decay like  $n^{-3}$ , so a truncation at about  $n = 50$  is adequately converged. Because (34) is singular at the equator,  $\hat{y}$  is shifted by a small amount,  $y_o = 0.05$ .

### b. The buoyancy field and the residual overturning circulation

Figure 3 shows buoyancy in the  $x$ - $y$  plane at different levels for the parameters given in Table 1. The buoyancy pattern below the surface shows a reversal with depth in the latitudinal gradient. This reversal is due to the buoyancy forcing (i.e., the reversal is qualitatively the same when  $\tau_0 = 0$ ) and is also obtained in models where the mean stratification,  $N^2$ , is determined as part of the solution (Colin de Verdière 1988). The reversal is most prominent on the eastern and southern sides of the basin.

The vertical structure of the buoyancy is illustrated in Fig. 4, which shows the endpoint values at the eastern and western boundaries and their difference,  $b_e - b_w$ . For the choice of parameters in Table 1 the total buoyancy,  $\bar{b} = b + N^2 z$ , is unstably stratified in the subpolar region, clearly violating the range of validity of the linearization procedure. With a larger value of  $N^2$ ,  $\bar{b}$  would be stably stratified everywhere, as is observed in the eddy-resolving simulation used as a comparison (cf. Wolfe and Cessi 2010, and Fig. 5). Although incapable of determining the basic stratification, the linear model indicates how  $N^2$  is established:  $N^2$  is such that the total buoyancy  $b + N^2 z$  is stably stratified everywhere. Since

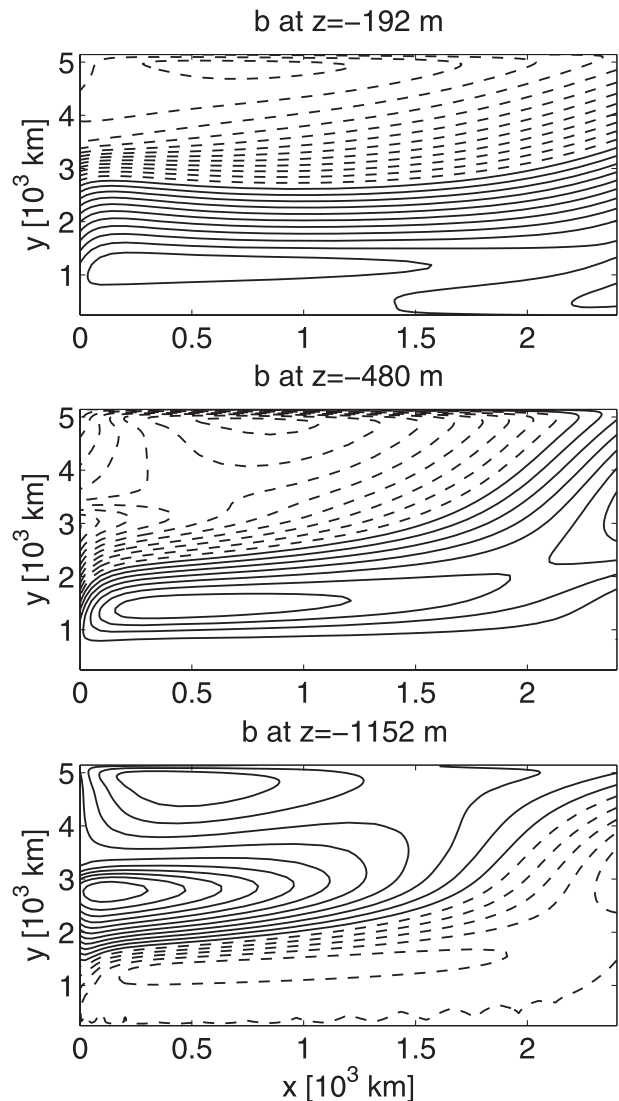


FIG. 3. Three plan views of the dimensional buoyancy for the linear solution (33) at various depths for the parameter values given in Table 1. Notice the reversal of the north-south buoyancy gradient at depth in the bottom panel, which can also be seen in the boundary values (cf. the two panels in Fig. 4). The contour interval is (top)  $1 \times 10^{-3} \text{ m s}^{-2}$ , (middle)  $0.5 \times 10^{-3} \text{ m s}^{-2}$ , and (bottom)  $2 \times 10^{-4} \text{ m s}^{-2}$ ; negative values dashed.

the buoyancy perturbation is most unstably stratified in the upper portion of the water column where the vertical scale of  $b$  is  $h_G$ , then  $N^2 \sim \Delta b/h_G$  in which  $\Delta b$  is the amplitude of the horizontal buoyancy difference in (15). As discussed in more detail in section 5,  $\Delta b$  can be proportional to  $B_0$  or  $\tau_0$ , according to which forcing dominates the solution. In general,  $\Delta b$  depends on both  $B_0$  and  $\tau_0$ .

To understand how the three-dimensional buoyancy structure is determined, it is useful to construct the

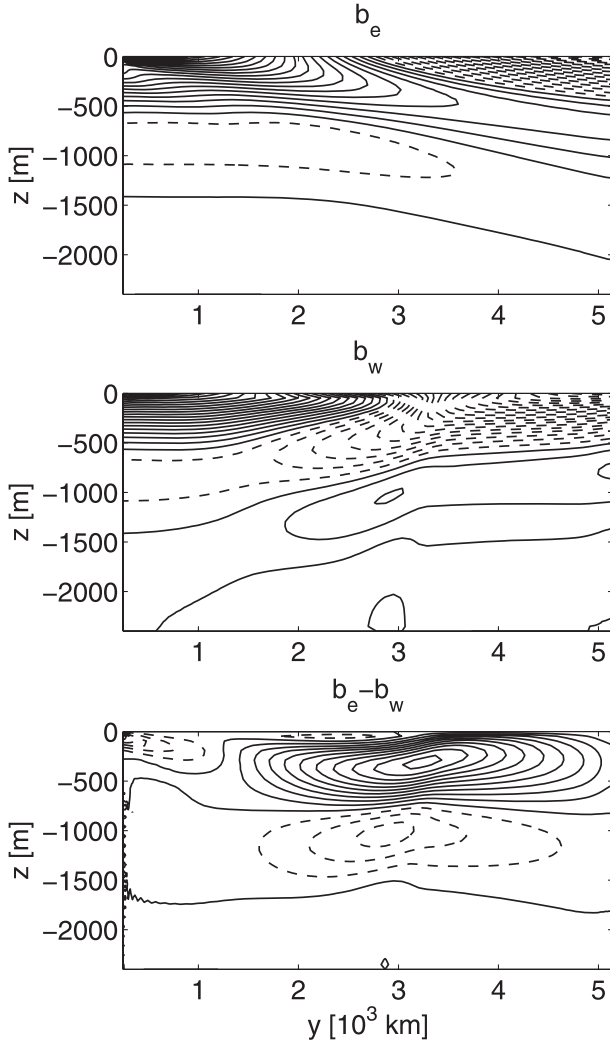


FIG. 4. (top) Bouyancy (top)  $b_e$  on the eastern boundary,  $x = x_e$ , for the same solution shown in Fig. 3; (middle)  $b_w$  on the western boundary,  $x = 0$ ; and (bottom) the difference  $b_e - b_w$ . The contour interval is  $2 \times 10^{-3} \text{ m s}^{-2}$ , negative values dashed.

residual circulation for the linear model. Using (4) to eliminate  $w$  from (5), we rewrite the buoyancy equation as

$$(N^2 \chi)_x + (N^2 \phi)_y = \kappa_v b_{zz}, \quad (36)$$

where we have defined the residual streamfunctions:

$$\chi \equiv - \int_{-H}^z u(x, y, \tilde{z}) d\tilde{z} + \psi b_y / N^2 - \kappa_e b_x / N^2 \quad (37)$$

and

$$\phi \equiv - \int_{-H}^z v(x, y, \tilde{z}) d\tilde{z} - \psi b_x / N^2 - \kappa_e b_y / N^2. \quad (38)$$

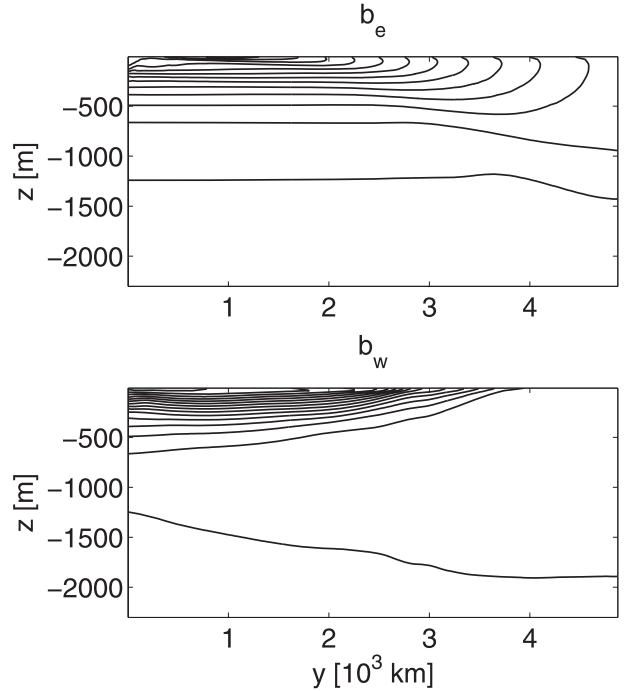


FIG. 5. Total buoyancy (top)  $b_e$  on the eastern boundary,  $x = x_e$ , for the Northern Hemisphere portion of the same eddy resolving described in Fig. 1 (cf. Wolfe and Cessi 2010) and (bottom)  $b_w$  on the western boundary,  $x = 0$ . A thermostat extends from north to south and from east to west, which contains the bulk of the residual and meridional overturning circulations. The contour interval is  $2 \times 10^{-3} \text{ m s}^{-2}$ .

In (36) the baroclinic flow is only advecting the basic buoyancy  $N^2 z$ , while the advection of horizontal buoyancy is effected by the barotropic flow only.<sup>4</sup> The residual flow in (37) and (38) is composed of three parts: the time-mean baroclinic flow; the “standing eddy” component due to the advection by the barotropic gyre of the perturbation buoyancy; and the eddy flux due to mesoscale eddies, parameterized as downgradient diffusion  $\kappa_e$ .

The formulation (36) makes it apparent that the effective boundary condition (14) conserves buoyancy. Taking (37), for example, the first and last terms on the right-hand side cancel on the eastern and western boundary and the second term on the rhs naturally vanishes on the boundaries. Likewise, in (38) the first and third terms on the rhs cancel on the northern and southern boundaries.

Figure 6 (top) shows  $\chi$  at  $y = 2020 \text{ km}$ : there is a clockwise circulation in the  $x$ - $z$  plane in the upper portion of the water column and an anticlockwise circulation below. Figure 6 (bottom) shows the Eulerian component

<sup>4</sup> If the advection of buoyancy perturbation by the baroclinic flow were included, this would be the additional term  $-(b_x \chi + b_y \phi)_z$  on the lhs of (36).

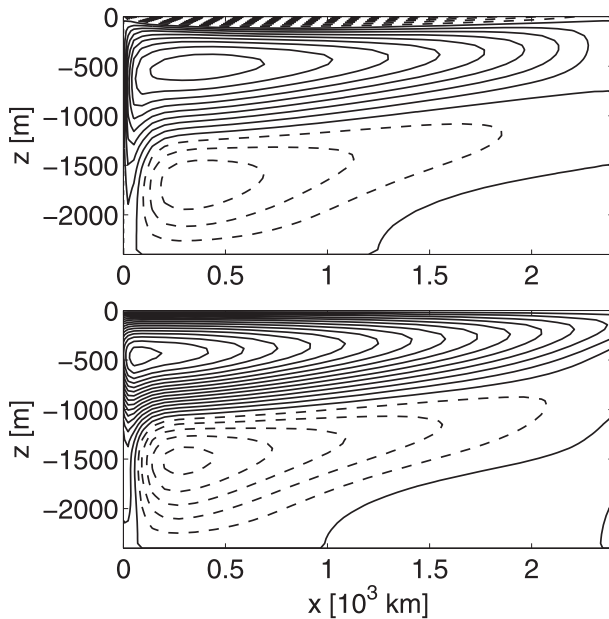


FIG. 6. (top) The residual streamfunction  $\chi$ , defined in (37), is contoured in the  $x$ - $z$  plane at  $y = 200$  km and (bottom) the Eulerian component of the streamfunction  $\chi$  (i.e.,  $-\int_{-H}^z u(x, y, \bar{z}) d\bar{z}$ ) is contoured in the  $x$ - $z$  plane at the same latitude. The contour level is  $0.2 \text{ m}^2 \text{ s}^{-1}$ , negative contours dashed.

of  $\chi$ . The most notable feature is a flow into and out of the east and west boundaries, which is compensated by the eddy flux of buoyancy, through the effective boundary conditions in (14). Because the zonal baroclinic flow is in geostrophic balance everywhere, any horizontal buoyancy (and pressure) gradient along the boundary is accompanied by flow into the effective boundary. This  $\mathbf{u} \cdot \mathbf{n} \neq 0$  is allowed, without violating mass and without altering the buoyancy balance, by the effective boundary condition, which returns the flow into the effective wall at a different level while leaving the buoyancy unchanged.

The clockwise cell and positive zonal shear in Fig. 6 are driven by the surface buoyancy diffused down to a depth of order  $h_G$  on the west and  $h$  on the east. Because of the meridional boundaries, there is downwelling at  $x = x_e$  and upwelling at  $x = 0$ . With the basic stratification  $N^2$ , the clockwise flow pushes buoyant fluid down on the east and dense fluid up on the west, causing a positive east-west buoyancy gradient and a meridional shear. This meridional shear is responsible for the meridional overturn, as shown in the top panel of Fig. 7 where we contour the ROC defined as

$$\Phi \equiv \int_0^{x_e} \phi dx, \quad (39)$$

where  $\phi$  is defined in (38). In turn,  $\Phi$  brings low buoyancy fluid up near the equator and high buoyancy fluid

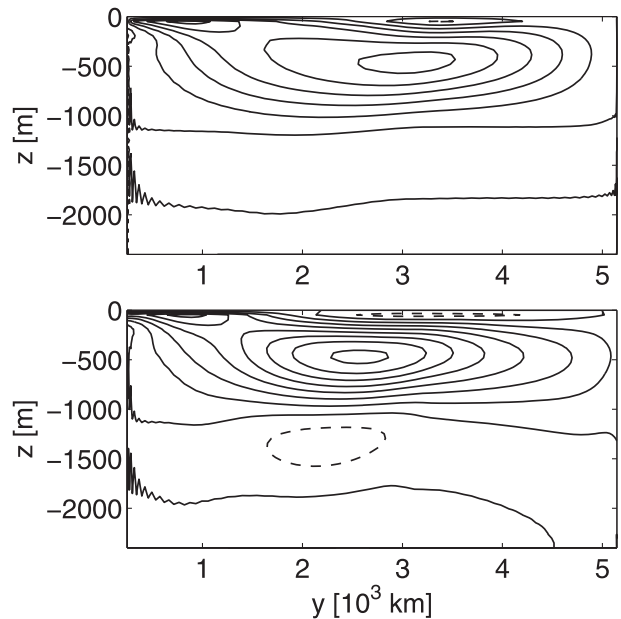


FIG. 7. (top) The residual overturning circulation  $\Phi \equiv \int_0^{x_e} \phi dx$ , with  $\phi$  defined in (38), is contoured in the  $y$ - $z$  plane. (bottom) The meridional overturning streamfunction  $\Psi$ , defined in (40), is contoured in the  $y$ - $z$  plane. The contour level is  $1 \times 10^6 \text{ m}^3 \text{ s}^{-1}$ , negative contours dashed.

down near the northern boundary, producing the reversal in the meridional buoyancy gradient seen in the bottom panel of Fig. 3. This reversed buoyancy gradient drives the anticlockwise cells seen in the bottom halves of Figs. 6 and 7. The zonal section shown in Fig. 6 is in the middle of the basin: farther south the anticlockwise cell expands until it occupies all of the water column; this expansion is consistent with the shoaling of the reversed meridional buoyancy gradients toward the southeast, seen in Fig. 3. The MOC contoured in Fig. 7 induces vortex compression (expansion) in the poleward half of the domain in the upper (lower) part of the water column. The equatorward half of the domain experiences the opposite pattern of vortex compression and expansion. This vortex stretching is accompanied by meridional flow in the interior of the basin, with a cyclonic (anticyclonic) gyre in the poleward half of the domain in the upper (lower) portion of the water column and a baroclinic gyre of the opposite sign in the equatorward half of the domain. This buoyancy-driven circulation is modified quantitatively, but not qualitatively, by the wind forcing.

The ROC,  $\Phi(y, z)$ , (Fig. 7, top) is weaker than the MOC (Fig. 7, bottom) because there is partial cancellation between the meridional mean flow and the advection by the barotropic flow, that is, between the first and second terms on the rhs of (38). Specifically, in the

subtropical gyre  $-\psi$  is negative while  $b_x$  is positive (negative) where the MOC is positive (negative), hence the partial cancellation. In the subpolar gyre  $-\psi > 0$  and the advection by the barotropic flow reinforces the Eulerian transport, shifting the maximum of  $\Phi$  north of the maximum of the MOC. These results are in qualitative agreement with the findings in the eddy-resolving computations described in Wolfe and Cessi (2010). In the eddy-resolving calculations, the reduction and northward shift in the maximum of the ROC compared to the MOC are even more pronounced because the flow in the upper portion of the column is larger (it occurs over the depth  $h_G$  rather than  $H$ ); furthermore, it is substantially augmented over the Sverdrup value by the presence of an inertial recirculation (cf. Figs. 15 and 18 of Wolfe and Cessi 2010).

The eddy-flux term is negligible except near the boundaries at  $y = 0$  and  $y = L$  where it allows some flow into the effective walls, accompanied by an alongshore buoyancy gradient. The eddy-flux term is also positive everywhere except close to the boundaries, contrary to the finding in our eddy-resolving computations, where there is upgradient buoyancy eddy transport in the western boundary current extension region (Wolfe et al. 2008). Clearly, upgradient eddy fluxes cannot be captured with a Gent–McWilliams-type parameterization.

*c. The meridional overturning circulation*

The largest component of the residual overturning circulation comes from the mean meridional velocity, one measure of which is  $\Psi$ , the meridional overturning circulation, defined as

$$\Psi_z \equiv - \int_{x_w}^{x_e} v \, dx. \tag{40}$$

Here  $\Psi$  can be obtained from the east–west buoyancy difference through the formula (cf. CW09)

$$f\Psi \approx \left(\frac{z}{H} + 1\right) \int_{-H}^0 d\tilde{z} \int_{-H}^{\tilde{z}} (b_e - b_w) \, dz - \int_{-H}^z d\tilde{z} \int_{-H}^{\tilde{z}} (b_e - b_w) \, dz + \int_0^{x_e} \left[ \tau - \left(\frac{z}{H} + 1\right) \tau \Big|_{z=0} \right] dx, \tag{41}$$

and its structure is shown in Fig. 7 (bottom). The MOC is dominated by the contribution from  $b_e - b_w$ , shown in Fig. 4, with the wind stress component important near the surface. An interesting feature of  $\Psi$  is the counterrotating cell below the thermally direct cell. In single-hemisphere or symmetric double-hemisphere domains there is no counterrotating cell below the main cell. This

is because these configurations have very weak intermediate and deep stratification. Without deep stratification, the thermally direct cell reaches all the way to the bottom ( $h, h_G \rightarrow \infty$ ) and no counterrotating cell develops. In our linearized model and in domains with two hemispheres with a circumpolar Southern Ocean, there is deep stratification that allows the development of a counterrotating cell. In double-hemisphere geometries the thermally indirect cell has been attributed to the transequatorial intrusion of the anticlockwise MOC from the opposite hemisphere (Klinger and Marotzke 1999). However, our model demonstrates that a counterrotating deep cell can also be driven by processes local to the Northern Hemisphere, in particular to the equatorial upwelling and subpolar downwelling associated with the main direct overturning cell. The presence of a Southern Hemisphere with a circumpolar portion is implied by our assumption that there is the deep stratification upon which the counterrotating cell relies.

**5. Scaling of the overturning cells**

In this section, we provide scaling laws for the meridional overturning cells obtained in the linear model. From (41) the amplitude of  $\Psi$  is proportional to the east–west buoyancy difference  $\Delta b$  and the square of a scale height  $D$ . In the following, we show that these two scales are different for the different cells seen in Fig. 7, leading to different scalings.

*a. The buoyancy-driven cells*

For the subsurface clockwise cell, seen in Fig. 7, the vortex stretching that balances the meridional flow is dominated by vertical diffusion of the surface buoyancy. Thus, the relevant amplitude is  $\Delta b = B_0$  and the scale height is  $D = h_G$  in (29). We thus have the scaling:

$$\Psi_{\max} \sim \frac{\Delta b h_G^2}{f} = B_0 \left( \frac{\kappa_v x_e}{N^2 \beta} \right)^{1/2}. \tag{42}$$

The scaling for  $\Psi_{\max}$  recovers both the diffusive and the internal thermocline regimes once the appropriate scaling for  $N^2$  is chosen (cf. Vallis 2000): in the diffusive regime stratification is set by diffusing buoyancy from the surface, that is,  $N^2 \sim B_0/h_G$ , so that  $h_G \sim (\kappa_v \beta L^2 x_e / B_0)^{1/3}$  and  $\Psi_{\max} \sim (\sqrt{B_0} \kappa_v \beta L^2 x_e)^{2/3}$ ; in the internal thermocline regime stratification is set by ventilation and homogenization, that is,  $N^2 \sim B_0/h_v$ , and  $\Psi_{\max} \sim (B_0 h_v \kappa_v \beta L^2 x_e)^{1/2}$ , with  $h_v$  given in (32).

Because  $h_G$  characterizes the vertical scale of  $b_w$ , it is tempting to conclude that  $b_e$  does not contribute to  $\Psi$ . However, comparison between the three panels of Fig. 4

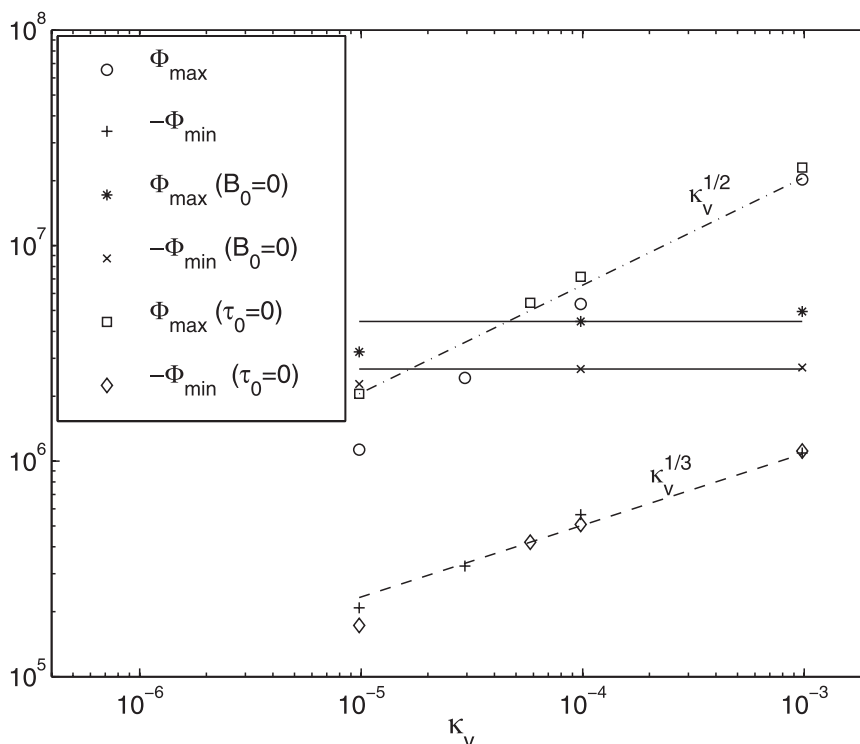


FIG. 8. The subsurface maximum (open circles and squares) and minimum (crosses and open diamonds) of  $\Phi$  are plotted as a function of the diapycnal diffusivity  $\kappa_v$ . We consider forcing by both the wind and buoyancy together (open circles and plus signs), buoyancy forcing alone (open squares and diamonds), and wind forcing alone (asterisks and crosses). For the wind-forcing-only cases (cf. Fig. 11), the absolute maximum and minimum are plotted. Lines of slope  $\kappa_v^{1/2}$  (dotted-dashed),  $\kappa_v^{1/3}$  (dashed), and  $\kappa_v^0$  (solid) are also plotted. All the other parameters are as in Table 1.

shows that both endpoint values contribute to  $b_w - b_e$ , especially at depth. As shown in the bottom panel of Fig. 3, the reversed buoyancy gradients are more prominent on the eastern side of the basin. In this region, laminar, eddyless theories would predict the “shadow zone” where no pressure gradient is allowed. Here, the effective boundary condition allows gradients along the eastern boundary, which, as shown by comparing the top and middle panels in Fig. 4, are transferred to the western boundary from  $b_e$  along the northern boundary of the domain so that reversed buoyancy gradients are found at both  $x = 0$  and  $x = x_e$ . The importance of the horizontal buoyancy gradients on the eastern boundary is also clear from Fig. 5: in the northern half of the domain  $b_e - b_w$  is all due to  $b_e$ .

Thus, the relevant depth scale for the deep minimum of the overturning is  $D = h$ , not  $D = h_G$ . We thus have the scaling

$$\Psi_{\min} \sim \frac{\Delta b h^2}{f} = B_0 \left( \frac{\kappa_e \kappa_v L}{N^4 \beta} \right)^{1/3} \quad (43)$$

so that the subsurface minimum scales like  $\Psi_{\min} \sim (\kappa_v \kappa_e)^{1/3}$ . Indeed, this scaling is obtained in the linear model when these two parameters are varied: in Fig. 8 only  $\kappa_v$  is varied, and the dependence on  $\kappa_e$  has been verified (figure not shown). This indicates that the gradients on the eastern boundary are essential for the existence of the counterrotating cell. To our knowledge, no scaling has been previously proposed for the counterrotating deep cell shown in Fig. 7.

The same scalings hold for the zonally integrated residual circulation  $\Phi$ , which satisfies the zonal integral of (36); that is,

$$N^2 \Phi_y = \kappa_v \int_0^{x_e} b_{zz} dx. \quad (44)$$

Thus,  $\Phi \sim N^{-2} \kappa_v \Delta b D^{-2} L_x L$ , where again  $\Delta b$  denotes the buoyancy difference,  $D$  the vertical scale, and  $L_x$  the zonal scale. The discussion for  $\Psi$  can be repeated for  $\Phi$ : for the subsurface maximum the relevant scales are  $D = h_g$ ,  $\Delta b = B_0$ , and  $L_x = x_e$  (circles, triangles, and

dashed-dotted line in Fig. 8). For the subsurface minimum, the relevant scales are  $D = h$ ,  $\Delta b = B_0$ , and  $L_x = l$  (crosses, diamonds, and dashed line in Fig. 8). Using the expressions for  $l$ ,  $h$ , and  $h_G$  shows that  $\Phi$  and  $\Psi$  have the same scalings.

The scalings (42) and (43) are valid for the case of a single hemisphere. When two hemispheres are present, nonlocal effects due to interhemispheric flows can add to the structure of the MOC and change the scalings. Indeed, the deep cell obtained in the linear model is weaker, shallower, and farther poleward than that obtained in the eddy-resolving model in a domain consisting of a semienclosed, double-hemisphere basin, with a reentrant region in the southernmost eighth of the domain [cf. Fig. 9 (top) and Wolfe and Cessi (2010)].

In the semienclosed domain used for the eddy-resolving computations, neither the thermally direct MOC nor the counterrotating cell obey the scalings (42) if there are shared surface buoyancy values between the Northern Hemisphere and the reentrant channel in the Southern Hemisphere. In fact, Wolfe and Cessi (2010) show that even the thermally direct northern MOC is driven nonlocally by dynamics in a southern channel analogous to Drake Passage. However, if the surface buoyancy distribution is such that the densest water formed in the Northern Hemisphere is lighter than any water formed in the channel [the “warm pole” cases of Wolfe and Cessi (2009, 2010)], then interhemispheric flows are weak but there is deep stratification. A secondary counterrotating cell then appears above the interhemispheric deep cell (cf. Fig. 9, bottom). This cell appears to be driven by the single-hemisphere dynamics described above. Indeed, the magnitude of this intermediate depth cell scales according to (42) (cf. Fig. 10). The maximum of the thermally direct MOC in the eddy-resolving model is influenced by an inertial recirculation near the western boundary current extension: this causes the upper MOC to develop a vertically elongated structure not seen in the linear model. Nevertheless, the scaling (42), with  $N^2$  appropriately chosen to account for the thermocline stratification in the internal thermocline regime, is verified in the eddy computations.

*b. The wind-driven overturning cells*

Above the large, thermally direct overturning cell shown in Fig. 7 (top and bottom) are two shallow cells, one thermally indirect north of the subtropics and the other thermally direct in the tropics. These are the wind-driven cells, whose surface branch is the Ekman flow—southward in the region of westerlies and northward in the region of easterlies. For the parameter values in Table 1,

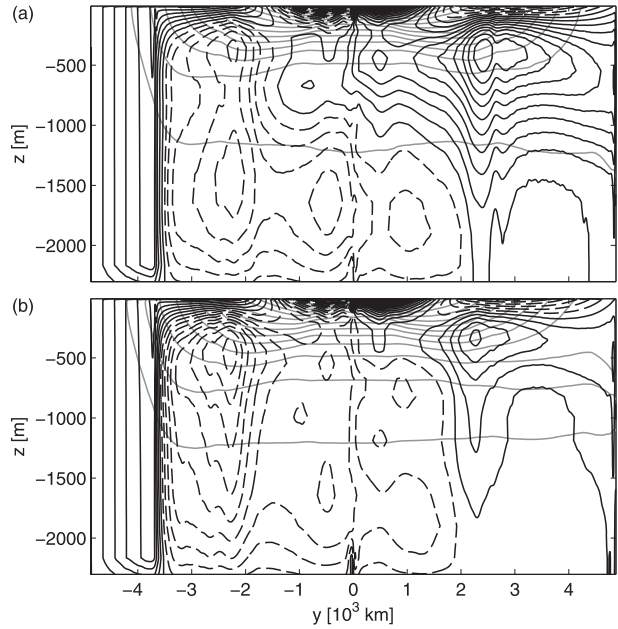


FIG. 9. The time-average meridional overturning streamfunction  $\Psi$  (thick lines) and the time-average buoyancy (thin gray lines) from the eddy-resolving model (two hemispheres with a channel in the southernmost eighth of the domain) for cases where the transequatorial overturning is (top) strong and (bottom) weak [experiments CP-k4 and WP-k4 of Wolfe and Cessi (2010), respectively]. A secondary counterrotating cell is visible (bottom panel) near 750 m depth in the subtropical Northern Hemisphere. The contour interval is  $0.5 \times 10^6 \text{ m}^3 \text{ s}^{-1}$  for the streamfunction and  $2 \times 10^{-3} \text{ m s}^{-2}$  for the buoyancy, negative contours dashed.

these cells are obscured by the dominantly buoyancy-driven overturn except near the surface.

These shallow cells are most clearly examined by suppressing the buoyancy forcing, that is, by replacing the top boundary condition with  $b = 0$  at  $z = 0$ . Buoyancy forcing still exists implicitly since we assume a prescribed background stratification  $N^2$ . The resulting overturning, with the parameters set as in Table 1 (except  $B_0 = 0$ ), is shown in Fig. 11.

The vertical and horizontal scales of the buoyancy perturbations are as in section 3, that is, (23), (29), and (30). However, the amplitude of the solution is now determined by the top boundary condition on the vertical velocity, which below the Ekman layer is approximately given by the Ekman pumping (G85); that is,

$$\frac{\kappa_v b_{zz}}{N^2} = w \approx w_E = -\left(\frac{\tau}{f}\right)_y \quad \text{at } z = 0. \quad (45)$$

This relation immediately gives the amplitude of the overturning since  $\Psi_y = \int_0^x w \, dx$ . Thus, the scaling of the shallow meridional overturning streamfunction  $\Psi_{\text{up}}$  is given by

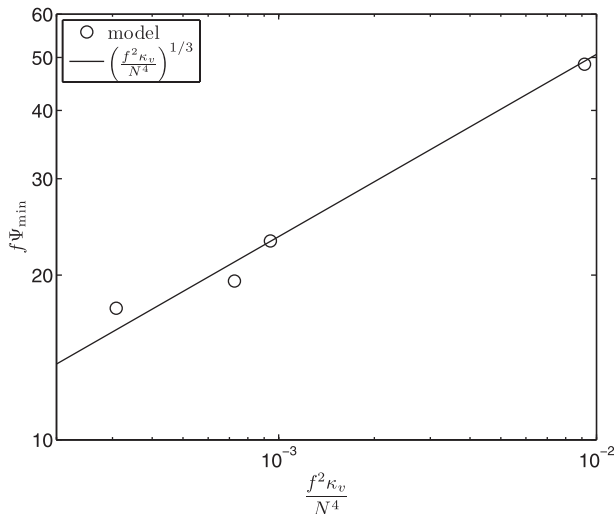


FIG. 10. Magnitude of the intermediate counterrotating cell  $\Psi_{\min}$  times the Coriolis parameter  $f(\circ)$  plotted as a function of the diapycnal diffusivity  $\kappa_v$ , scaled by  $f^2/N^4$  for the eddy-resolving model in the warm pole configuration shown in Fig. 9 (bottom). Also plotted is a line of slope  $(f^2\kappa_v/N^4)^{1/3}$ .

$$\Psi_{\text{up}} \sim w_E L x_e, \quad (46)$$

independent of the diapycnal diffusivity. This scaling has been confirmed in the linear model (asterisks and multiply symbols in Fig. 8). The scaling for  $\Phi$  forced by the wind only, with  $B_0 = 0$ , closely follows the arguments given for  $\Psi$ , applied to (44), and we find that the amplitude of the shallow, wind-driven residual cells is also given by

$$\Phi_{\text{up}} \sim w_E L x_e. \quad (47)$$

The wind-driven thermally indirect surface cell, characterized by  $\Psi_{\text{up}}$  and  $\Phi_{\text{up}}$ , goes in the direction opposite to the thermally direct buoyancy-driven cell and, when the amplitudes become comparable, some cancellation occurs between the two: thus, the buoyancy and local wind stress forcing compete in the scalings for both the MOC and the ROC. When the contributions from both become comparable, the individual scalings are obscured, leading to an apparent steeper scaling, which is simply a superposition of two competing power laws. For the range of parameters examined here, the wind-driven cells are subdominant for most values of diffusivity shown in Fig. 8, but they become comparable for the lowest value of diffusivity.

## 6. Summary and discussion

A model of the thermocline linearized around prescribed basic stratification,  $N^2$ , and the wind-driven, barotropic flow gives remarkably realistic buoyancy and

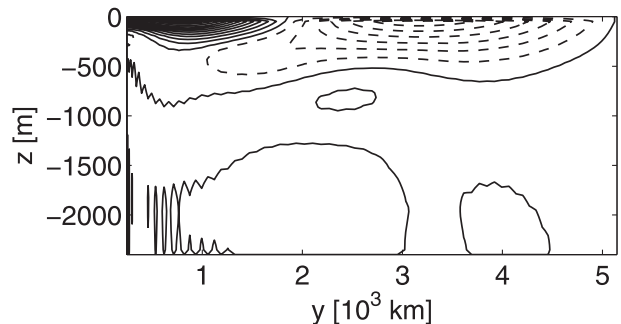


FIG. 11. The overturning streamfunction  $\Psi$ , without surface buoyancy forcing: that is, when the parameters are as in Table 1 except that  $B_0 = 0$ . The contour interval is  $4 \times 10^5 \text{ m}^3 \text{ s}^{-1}$ , negative values dashed.

zonally averaged meridional transports when effective boundary conditions are used. The effective boundary conditions require that the residual flow normal to the boundary vanishes but not the individual Eulerian and eddy components. There can be an exchange between these two components inside the “effective coast” (i.e., inside the unresolved viscous, nonhydrostatic layers) while conserving mass and buoyancy. This process enables realistic buoyancy gradients along all boundaries in a quasi-adiabatic, inviscid regime.

Especially important in the context of the MOC is the value of the buoyancy on the eastern boundary,  $b_e(y, z)$ , since it is the difference between  $b_e$  and the buoyancy on the western wall  $b_w(y, z)$  that geostrophically maintains the zonally averaged meridional velocity. Although the main thermally direct overturning cell is on the same vertical scale as  $b_w$ ,  $b_e$  makes a comparable contribution.

The linear model provides clear scalings for the MOC and allows us to separately identify the contribution from the buoyancy and wind-driven forcing. The buoyancy forcing and the wind stress compete in driving the main overturning cell: the buoyancy forces a thermally direct surface cell and the wind stress a thermally indirect one. The main contribution to these surface cells occurs on the horizontal scales dictated by the surface forcing, which in our case are the scales of the basin. Thus, the vertical scale of the buoyancy is the Gill depth  $h_G$ , defined in (29).

There is also a buoyancy-driven counterrotating cell at depth associated with a deep reversed north–south buoyancy gradient. Previously, this cell has been attributed to the cross-equatorial intrusion of the MOC from the opposite hemisphere, formed with denser water (e.g., Vallis 2000). Here we show that a counterrotating cell can also be locally driven, as long as there is stratification at depth. Well below the surface, the horizontal scale of the buoyancy is internally determined

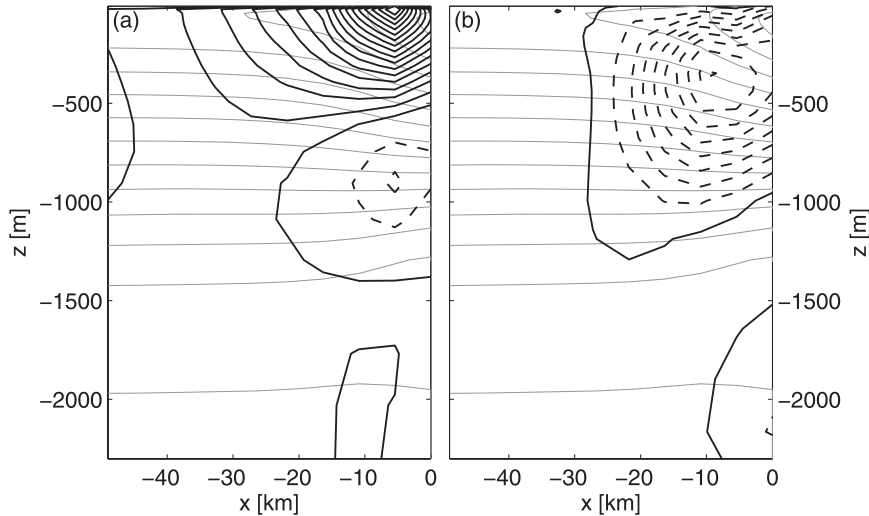


FIG. 12. Temperature (gray contours), (a) meridional velocity (black contours), and (b) vertical velocity (contours) near the eastern boundary in the middle of the northern subpolar gyre for the eddy-resolving model. The contour intervals for temperature, meridional velocity, and vertical velocity are  $0.25^{\circ}\text{C}$ ,  $2.5 \text{ cm s}^{-1}$ , and  $0.25 \text{ mm s}^{-1}$ , respectively; negative contours are dashed. The origin of  $x$  has been shifted to the eastern boundary.

and is dominated by the scale at the eastern boundary,  $l$ , so that the vertical scale is  $h$  [both scales are defined in (23)]. Therefore, the strength of this cell depends, inter alia, on the “eddy diffusivity”  $\kappa_e$ , which in this model is externally prescribed.

A weakness of the linear formulation is that the basic stratification  $N$  must be prescribed, so the model is not completely predictive.<sup>5</sup> However, our understanding of the basic stratification is now quite advanced, and we have two mechanisms that have been clearly established: ventilation and homogenization (Luyten et al. 1983; Rhines and Young 1982) and diffusion (Welander 1971; G85). Thus, we can use these established results to extend our scalings to the nonlinear regime and recover the published scalings (Vallis 2000). A third mechanism, remote control of  $N^2$  by the dynamics of the Southern Ocean, has also been proposed (Samelson 2009; Wolfe and Cessi 2010), and this is naturally considered by our formulation with prescribed stratification.

Another weakness of the present model is that it is pivoted around geostrophy and thus cannot accommodate a transequatorial domain [(15) is singular at the equator]. Therefore, all nonlocal processes that contribute to stratification and the MOC cannot be captured. In particular, the contribution to the MOC of the pole-to-pole circulation is missed in a single-hemisphere formulation.

<sup>5</sup> We note that, although our formulation is linearized, we have used values of the parameters well beyond the range of validity of the linear approximation.

Although the linear model has some natural horizontal scales,  $l$  and  $\delta_p$ , these are not representative of the eastern and western boundary currents found in the eddy-resolving model that we have used for comparison. This is painfully apparent if one compares  $l \sim 10^3 \text{ km}$  with the 30-km eastern boundary layer scale found in eddy-resolving models (cf. Fig. 12). We conjecture that there are two reasons for this discrepancy: first, the divergence of eddy momentum flux cannot be neglected near the boundaries, and it could provide an alternative scale for the eastern boundary current; second, the advection by the baroclinic component of the velocity has been neglected. The top panel of Fig. 6 shows that the typical east–west flow is toward the eastern boundary in the upper part of the water column. This flow might help to confine the buoyancy signal near the boundary, especially in the poleward half of the domain, leading to the formation of the narrow current seen in Fig. 12.

Finally, although we have not examined the time-dependent problem, our steady-state results suggest that the variability of the MOC will have substantial contributions from the time dependence of both  $b_e$  and  $b_w$ . In particular, we anticipate that the MOC variability from the eastern boundary would receive comparable contributions from the wind stress and from the surface buoyancy since the intrinsic vertical and horizontal scales of the response are the same for both processes.

*Acknowledgments.* This research was supported by the Office of Science (BER), U.S. Department of Energy, Grants DE-FG02-01ER63252 and DE-SC0001963.

We acknowledge the National Center for Computational Sciences at Oak Ridge National Laboratory, San Diego Super Computer Center, and NERSC for computational resources used in support of this project. David Marshall and an anonymous reviewer are thanked for their insightful, detailed, and constructive comments.

## REFERENCES

- Barcilon, V., and J. Pedlosky, 1967: A unified theory of homogeneous and stratified rotating fluids. *J. Fluid Mech.*, **29**, 609–621.
- Cessi, P., and C. L. Wolfe, 2009: Eddy-driven buoyancy gradients on eastern boundaries and their role in the thermocline. *J. Phys. Oceanogr.*, **39**, 1595–1614.
- Colin de Verdière, A., 1988: Buoyancy driven planetary flows. *J. Mar. Res.*, **46**, 215–265.
- , 1989: On the interaction of wind and buoyancy driven gyres. *J. Mar. Res.*, **47**, 595–633.
- Cox, M. D., and K. Bryan, 1984: A numerical model of the ventilated thermocline. *J. Phys. Oceanogr.*, **14**, 674–687.
- Gent, P., and J. C. McWilliams, 1990: Isopycnal mixing in ocean circulation models. *J. Phys. Oceanogr.*, **20**, 150–155.
- Gill, A. E., 1985: An explicit solution of the linear thermocline equations. *Tellus*, **37A**, 276–285.
- Gnanadesikan, A., 1999: A simple predictive model for the structure of the oceanic pycnocline. *Science*, **283**, 2077–2079.
- Hirschi, J., and J. Marotzke, 2007: Reconstructing the meridional overturning circulation from boundary density and the zonal wind stress. *J. Phys. Oceanogr.*, **37**, 743–763.
- Kanzow, T., and Coauthors, 2008: A prototype system of observing the Atlantic meridional overturning circulation: Scientific basis, measurement and risk mitigation strategies, and first results. *J. Oper. Oceanogr.*, **1**, 19–28.
- , H. Johnson, D. Marshall, S. A. Cunningham, J. J.-M. Hirschi, A. Mujahid, H. L. Bryden, and W. E. Johns, 2009: Basinwide integrated volume transports in an eddy-filled ocean. *J. Phys. Oceanogr.*, **39**, 3091–3110.
- Klinger, B. A., and J. Marotzke, 1999: Behavior of double-hemisphere thermohaline flows in a single basin. *J. Phys. Oceanogr.*, **29**, 382–399.
- Luyten, J., J. Pedlosky, and H. Stommel, 1983: The ventilated thermocline. *J. Phys. Oceanogr.*, **13**, 292–309.
- Pedlosky, J., 1969: Linear theory of the circulation of a stratified fluid. *J. Fluid Mech.*, **35**, 185–205.
- , and W. R. Young, 1983: Ventilation, potential vorticity homogenization and the structure of the ocean circulation. *J. Phys. Oceanogr.*, **13**, 2020–2037.
- Rhines, P. B., and W. R. Young, 1982: A theory of the wind-driven circulation. I. Mid-ocean gyres. *J. Mar. Res.*, **40** (Suppl.), 559–596.
- Salmon, R., 1986: A simplified linear ocean circulation theory. *J. Mar. Res.*, **44**, 695–711.
- , 1990: The thermocline as an “internal boundary layer.” *J. Mar. Res.*, **48**, 437–469.
- Samelson, R. M., 2009: A simple dynamical model of the warm-water branch of the middepth meridional overturning cell. *J. Phys. Oceanogr.*, **39**, 1216–1230.
- , and G. K. Vallis, 1997: Large-scale circulation with small diapycnal diffusion: The two-thermocline limit. *J. Mar. Res.*, **55**, 223–275.
- Smith, K. S., and G. K. Vallis, 2001: The scales of equilibration of mid-ocean eddies: Freely evolving flow. *J. Phys. Oceanogr.*, **31**, 554–571.
- Stommel, H., 1948: The westward intensification of wind-driven ocean currents. *Eos, Trans. Amer. Geophys. Union*, **29**, 202–206.
- , and J. Webster, 1962: Some properties of the thermocline equations in a subtropical gyre. *J. Mar. Res.*, **44**, 695–711.
- Trefethen, L. N., 2000: *Spectral Methods in MATLAB*. SIAM, 162 pp.
- Vallis, G. K., 2000: Large-scale circulation and production of stratification: Effects of wind, geometry, and diffusion. *J. Phys. Oceanogr.*, **30**, 933–954.
- Welander, P., 1971: The thermocline problem. *Philos. Trans. Roy. Soc. London*, **270A**, 415–421.
- Wolfe, C. L., and P. Cessi, 2009: Overturning circulation in an eddy-resolving model: The effect of the pole-to-pole temperature gradient. *J. Phys. Oceanogr.*, **39**, 125–142.
- , and —, 2010: What sets the strength of the middepth stratification and overturning circulation in eddying ocean models? *J. Phys. Oceanogr.*, **40**, 1520–1538.
- , —, J. L. McClean, and M. E. Maltrud, 2008: Vertical heat transport in eddying ocean models. *Geophys. Res. Lett.*, **35**, L23605, doi:10.1029/2008GL036138.
- Young, W. R., and P. B. Rhines, 1982: A theory of the wind-driven circulation. II. Circulation models and western boundary layers. *J. Mar. Res.*, **40**, 849–872.
- , and G. Ierley, 1986: Eastern boundary conditions and weak solutions of the ideal thermocline equations. *J. Phys. Oceanogr.*, **16**, 1884–1900.